

Full-scale tests of two-story RC frames retrofitted with steel plate multi-slit dampers

Mohammad Mahdi Javidan^a, Mohammad Seddiq Eskandari Nasab^b and Jinkoo Kim^{*}

Department of Civil & Architectural Engineering, Sungkyunkwan University, Suwon, Republic of Korea

(Received April 26, 2020, Revised May 13, 2021, Accepted May 17, 2021)

Abstract. There is a growing need of seismic retrofit of existing non-seismically designed structures in Korea after the 2016 Gyeongju and 2017 Pohang earthquakes, especially school buildings which experienced extensive damage during those two earthquakes. To this end, a steel multi-slit damper (MSD) was developed in this research which can be installed inside of partition walls of school buildings. Full-scale two-story RC frames were tested with and without the proposed dampers. The frames had structural details similar to school buildings constructed in the 1980s in Korea. The details of the experiments were described in detail, and the test results were validated using the analysis model. The developed seismic retrofit strategy was applied to a case study school building structure, and its seismic performance was evaluated before and after retrofit using the MSD. The results show that the developed retrofit strategy can improve the seismic performance of the structure to satisfy a given target performance level.

Keywords: seismic retrofit; slit dampers; energy dissipation; seismic performance; hysteretic damper

1. Introduction

The 2016 Gyeongju earthquake with the magnitude of 5.8 Mw followed by the 2017 Pohang earthquake with the magnitude of 5.4 Mw were among the strongest earthquakes in the recent history of Korea. As the two earthquakes caused significant damage in many structures including old school buildings, there is a growing need to develop efficient seismic retrofit schemes for school buildings and public facilities not designed for seismic loads. A photo of a school building damaged in the aftermath of the 2017 Pohang earthquake is shown in Fig. 1.

In addition to conventional seismic retrofit techniques such as adding shear walls, steel bracing, and column jacketing (Bahrani *et al.* 2019), there are relatively new techniques using energy dissipation devices including friction dampers (Lee and Kim 2015, Javidan and Kim 2019a, Yousef-beik *et al.* 2020a, b), buckling restrained braces (Kim *et al.* 2004, 2009; Lee *et al.* 2008, Park *et al.* 2012, Shin *et al.* 2012, Mohammadi *et al.* 2020a, b), base isolation (Xu 2009, Xu *et al.* 2016, 2019), viscoelastic dampers (Kim and Bang 2002, Choi and Kim 2010, Javidan and Kim 2020a, Xu *et al.* 2020), hysteretic or metallic dampers (Tsai *et al.* 1993, Whittaker *et al.* 1991, Kim 2019, Javidan and Kim 2020b), etc. Among these energy dissipation devices, steel slit dampers have an important position due to their stable energy dissipation capacity and relatively easy and cheap manufacture. Chan and Albermani

(2008) carried out cyclic loading test of steel slit dampers made from wide flange sections and verified their seismic energy dissipation capacity. Saffari *et al.* (2013) developed a slit damper for enhancing strength and ductility of post-Northridge connections. Lee and Kim (2015) carried out seismic performance evaluation of moment frames with slit dampers, and found that they were very effective in increasing seismic capacity of a framed structure. Lee and Kim (2017) proposed box-shaped steel slit dampers for seismic retrofit of building structures and verified their energy dissipation capability through a series of experiments. Nouredin *et al.* (2018) developed an optimum distribution technique of steel slit hybrid dampers based on life cycle cost. Naeem and Kim (2019) proposed a multi-slit damper (MSD) and verified its energy dissipation capacity using cyclic loading tests of the device.

MSD includes a weak and a strong slit damper connected in series. Each damper is made of steel plates with vertical slits which act as fuse under lateral deformation and dissipate seismic energy. The weak damper works at smaller drifts and its further deformation is prevented at a predefined drift using a gap closure mechanism, and then a strong slit damper is activated at larger drifts. Hence, the damper provides two step yield forces and a fail-safe mechanism to prevent fracture of the slits.

In this research the MSD was further investigated both analytically and experimentally to apply it in practice. The analytical model of the damper was developed based on the test results of the previous study (Naeem and Kim 2019). In addition, a series of tests was carried out on a planar two-story reinforced concrete (RC) frames to validate their applicability in real structures. Totally, three frames were tested, one bare frame and two frames retrofitted with MSDs having two different expected maximum capacities.

*Corresponding author, Professor
E-mail: jkim12@skku.edu

^aPostdoctoral researcher

^bPh.D. Student



Fig. 1 A damaged school building after the 2017 Pohang earthquake (photo by corresponding author)

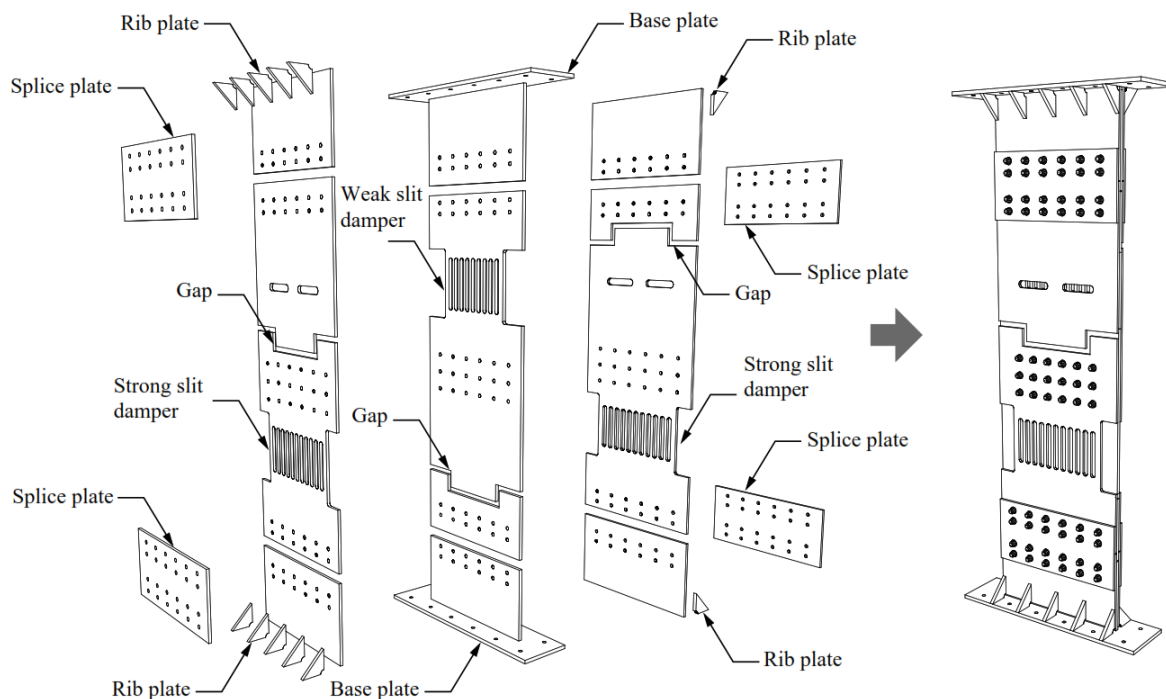


Fig. 2 Assembly of multi-slit damper

The member sizes and structural details of this benchmark frame were taken from typical school building constructed in the 1980s in Korea which were proven to be vulnerable in recent earthquakes.

The seismic performances of the two-story RC frames were assessed through cyclic loading test according to ACI 374 (ACI 2005). Experimental results were explained in detail and the behavior of the retrofitted frames were compared with that of the bare frame. The behaviors of the damper and connections were further evaluated using test and analysis results. The efficiency of the MSD in seismic retrofit was validated by applying it to an analysis model of a school building. The seismic performance of the model structure was evaluated before and after retrofit, and the results were compared in terms of maximum inter-story drift ratio, residual displacement, and energy dissipation.

2. Analysis model of the multi-slit damper

In this section the details of the MSD were described first, then the theoretical formulation of the damper was further developed from the previous research of Naem and Kim (2019). Based on the theoretical formulation, the analytical macromodel of the damper was provided for application in seismic retrofit design of structures. The accuracy of its hysteretic behavior was verified using the cyclic loading test of the damper.

The multi-slit damper (MSD) is a metallic seismic energy dissipation device which consists of two slit parts, namely a weak slit damper and a strong slit damper which are connected in series as shown in Fig. 2. The vertical slit columns act as sacrificial fuses under lateral deformations dissipating seismic energy. Each MSD is located between

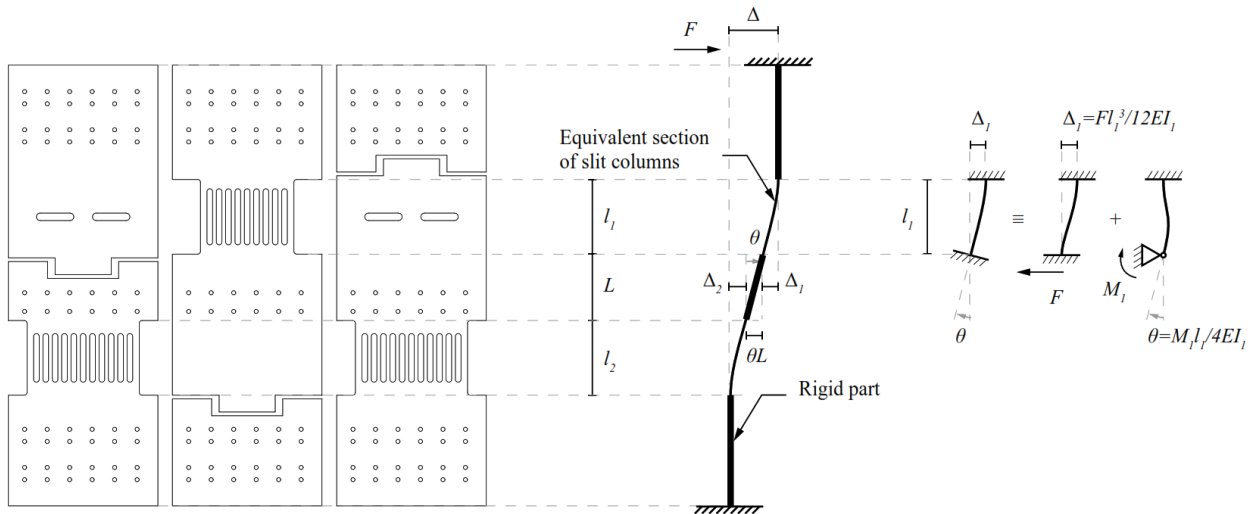


Fig. 3 Simplified approach for calculating elastic stiffness of MSD

two consecutive story beams of a structure and is activated by relative story displacements or inter-story drifts. The weak slit damper has a smaller stiffness and yield capacity, and therefore the weak slit part is activated first at small drifts. There are two plates parallel to the weak slit damper with gaps which are closed at a predefined drift, thus limiting the deformation of the weak slit damper and activating the strong slit damper. The strong slit damper has higher capacity and therefore at larger drifts more energy dissipation is provided without failure of the weak slit damper. The strong slit damper is composed of two steel plates to provide larger yield capacity. There is also a steel plate with gap parallel to the strong slit damper which provides a fail-safe mechanism preventing fracture of slit columns in the occurrence of excessively large inter-story drifts. The MSD can be manufactured with monolithic steel plates bolted at designated points, or it can be built with separate plates connected using splice plates as in the case of the test specimens in this research. In order to prevent out-of-plane deformations and constrain torsion of the MSD, several rib plates were welded to the MSD and the base plates.

In order to formulate the behavior of the MSD, its overall elastic stiffness and the capacity of weak and strong slit dampers need to be determined. Capacity of slit dampers can be found simply using plastic analysis, while the elastic stiffness of the MSD considering all details is hard to formulate. To this end, the parts consisting of three plates bolted to each other were assumed to act rigidly compared to the slit dampers as shown in Fig. 3. In that case, the overall deformation of the MSD is attributed to the relative displacement and rotation at the ends of the slit dampers.

The total displacement of the MSD is expressed as

$$\Delta = \Delta_1 + \theta L + \Delta_2 \quad (1)$$

where Δ_1 and Δ_2 as shown in Fig. 3 are the relative displacement at the ends of the weak and strong slit dampers, respectively, θ is the rigid body rotation of the

plates between the weak and strong slit damper, and L is the length of this plates. Previously Naeem and Kim (2019) determined the elastic stiffness of the MSD taking into consideration only the relative displacement at the ends of the slit dampers, which was refined in this study to increase the accuracy. When the whole system acts elastically the relative displacement of the weak slit damper is determined as

$$\Delta_1 = \frac{F l_1^3}{12 E I_1} \quad (2)$$

where F is the applied force, l_1 is the length of slit columns, E is the modulus of elasticity, and I_1 is the moment of inertia. The moment of inertia of the weak slit damper is

$$I_1 = \frac{t_1 \sum_{j=1}^n b_j^3}{12} \quad (3)$$

where t_1 is the plate thickness of the weak slit damper, b is the width of each slit column, and n is number of slit columns. Δ_2 can be also obtained in the similar way.

The rotation at the end of the slit dampers can be found by calculating the moments acting on the dampers and their rotational stiffness as depicted in Fig. 3. The two moment actions considering their signs can be found using the equilibrium equation and the equal rotation at the end of the weak and strong slit dampers

$$\begin{cases} M_1 - M_2 = FL \\ M_1/k_{\theta_1} + M_2/k_{\theta_2} = 0 \end{cases} \quad (4)$$

where M_1 and M_2 are the moments acting on the end of dampers, k_{θ_1} and k_{θ_2} are the rotational stiffness of the weak and strong slit dampers which are $4EI_1/l_1$ and $4EI_2/l_2$, respectively. After solving this system of equations, the bending moments can be derived as follows: $M_1 = FL/(1 + k_{\theta_2}/k_{\theta_1})$ and $M_2 = -FL/(1 + k_{\theta_1}/k_{\theta_2})$. The rotation is found to be $\theta = FL/(k_{\theta_1} + k_{\theta_2})$. By substituting the relative displacements at the ends, rotation, and rotational stiffnesses in Eq. (1), the total elastic

Table 1 Properties of tested MSD

Damper	Thickness t_i	Slit column length l_i	Slit column width b_j	Gap	Shear stiffness k_s	Rotational stiffness k_θ	Yield force
Weak	20 mm	270 mm	$2 \times 35 \text{ mm} + 8 \times 20 \text{ mm}$	30 mm	$32 \frac{\text{kN}}{\text{mm}}$	$776 \frac{\text{kN.m}}{\text{rad}}$	51 kN
Strong	$2 \times 15 \text{ mm}$	230 mm	$2 \times 35 \text{ mm} + 10 \times 20 \text{ mm}$	30 mm	$86 \frac{\text{kN}}{\text{mm}}$	$1513 \frac{\text{kN.m}}{\text{rad}}$	102 kN

displacement for a lateral force F is obtained as

$$\Delta = \frac{Fl_1^3}{12EI_1} + \frac{FL^2l_1l_2}{4E(I_1l_2 + I_2l_1)} + \frac{Fl_2^3}{12EI_2} \quad (5)$$

The elastic stiffness of the MSD is therefore equal to

$$\frac{1}{K} = \frac{l_1^3}{12EI_1} + \frac{L^2l_1l_2}{4E(I_1l_2 + I_2l_1)} + \frac{l_2^3}{12EI_2} \quad (6)$$

Based on the formulas derived above, the inflexion point of the MSD before yielding of the weak slit damper is between the weak and the strong slit dampers, approximately closer to the weaker one. After yielding of the weak slit damper, the inflexion point is located at the mid height of the weak slit damper where the moment is equal to zero. By knowing the location of inflexion point, the moment reactions acting on the fixed supports of the MSD can be found easily. The applied force is multiplied by the distance from the fixed end supports to the inflexion point to derive the bending moment used for the design of connections and base plate. By increasing the displacement after yielding of the weak slit damper, the gaps placed at the two outer faces are closed. Then further deformation of the weak slit damper is restricted and another force is transferred from the upper support to the strong slit damper which eventually leads to its yielding.

The yield force of the slit dampers can be determined based on the full plastic mechanism of slit columns [15]. The yield force of the i th slit damper is expressed as

$$F_{y,i} = \frac{2 \sum_{j=1}^n M_{p,j}}{l_i} \quad (7)$$

where l_i is the length of slit columns as depicted in Fig. 3, $M_{p,j}$ is the in-plane full plastic moment of the j th slit column calculated by

$$M_{p,j} = \sigma_{y,i} \frac{t_i b_j^2}{4} \quad (8)$$

where $\sigma_{y,i}$ is the yield strength of steel, b_j is the width of the j th slit column, t_i is the plate thickness of the i th slit damper.

In order to apply the MSD to structure models for seismic evaluation, a macromodel is established as shown in Fig. 4 which takes into account the behavior and reactions of the MSD. The model is established based on the elements available in the commercial software *SAP2000*® (CSI 2017) which is widely applied in practice. It is worthwhile to note that because of simplifications macromodels may not be able to exactly capture the

complex behavior of the MSD like detailed finite element models. However, macromodels provide computational efficiency which is required for application in practice (Usefi *et al.* 2018).

The slit dampers are modeled using the plastic wen element to allow for the smooth transition from elastic to plastic region, although multilinear plastic element can be employed as well. Their elastic stiffnesses are calculated using the first and third term of Eq. (6) and the yield forces are determined using Eq. (7). The rotation at the end of the slit dampers is modeled using elastic rotational springs as depicted in Fig. 4. As mentioned earlier, the stiffness of these springs, namely $k_{\theta 1}$ and $k_{\theta 2}$, are respectively $4EI_1/l_1$ and $4EI_2/l_2$ for the weak and strong slit dampers. By considering the stiffnesses in this way the overall elastic stiffness of the MSD is found to be equal to Eq. (6).

The gap closure mechanism is modeled using the hook and gap elements for restricting excessive deformation of the weak slit damper in the positive and negative directions. The second gap for the fail-safe mechanism of the strong slit damper can be modeled as well, but the drifts after retrofit will be limited to much smaller values, thus not considered in the model.

The parts with three plates bolted together is assumed to act as a whole section, thus modeled using frame element with a rectangular section. The deformation due to these parts are negligible as a result of large section height and thickness.

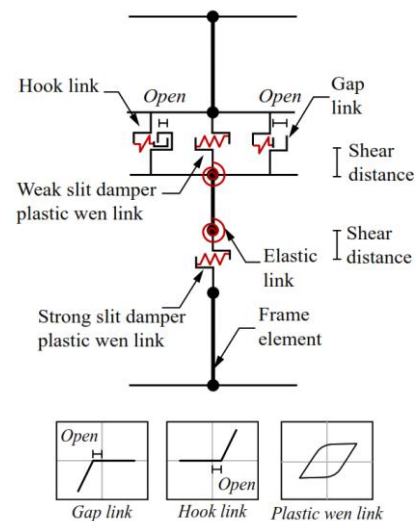


Fig. 4 Analytical model of MSD

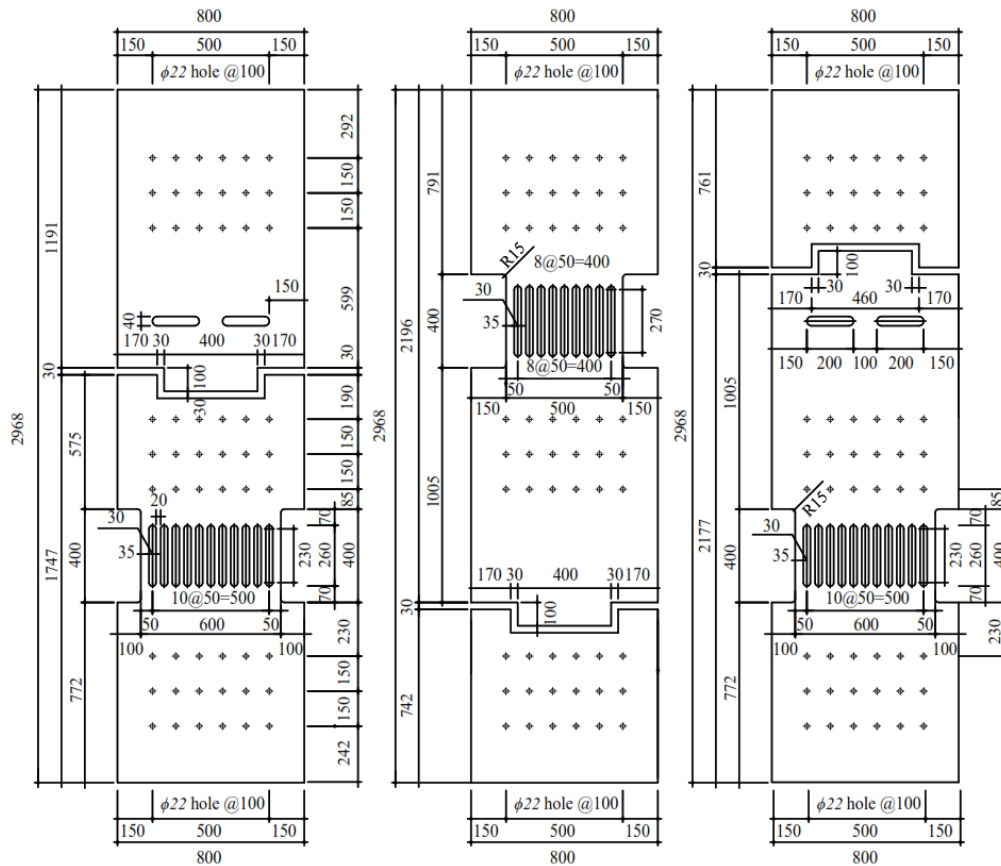


Fig. 5 Dimensions of the MSD tested by Naem and Kim (2019)

The parameter of shear distance is important to be considered due to the moment reaction of the MSD, although the horizontal reaction of the damper remains the same. When the slit damper reaches its full capacity, an inflexion point is formed at the mid-height of the slit columns where the moment is equal to zero. The shear distance parameter in the element properties should be defined accordingly.

The analysis model described above was verified using the experimental data obtained from the cyclic loading test of the MSD (Naem and Kim 2019). The details of this damper unit test were briefly described below. As shown in Fig. 5, the overall height of the test specimen is 2968 mm and the length of slit columns in the weak and strong slit dampers are respectively 270 mm and 230 mm. The rigid distance between the two dampers, L , is 605 mm. The plate thicknesses of the weak and strong slit dampers are 20 mm and 15 mm, respectively. The details of the damper specimen including the width of the slit columns, nominal yield strength, and the elastic stiffness are summarized in Table 1.

The MSD specimen was subjected to the cyclic loading specified in ASCE 41-13 (2013), and the applied force to the damper against the displacement was obtained. The average yield strength of steel is 242 MPa while the ultimate strength is 315 MPa. Based on these properties the nominal capacity of the weak and strong slit dampers were initially estimated to be 51 kN and 102 kN,

respectively. However, it was observed that because of the overstrength,

post-yield stiffness, and the formation of tension field at large displacement, the maximum capacity of the MSD reached 90 kN for the weak slit damper and 200 kN for the strong slit damper. These variations and uncertainties associated with the test results can be further quantified and taken into consideration using the probabilistic and fuzzy random analyses (Javidan *et al.* 2018, Javidan and Kim 2019b), which is not within the scope of the current study.

The analysis model of the damper was established based on the abovementioned details and the test data. The shear distance of both weak and strong slit dampers is 200 mm, which is the mid-height of the slit columns. A yield exponent of 1.0 and a post yield stiffness ratio of 2% were considered for the plastic Wen model to adequately capture the smooth yielding and post-yield behavior. The stiffness of the damper was estimated based on the formulas derived above while the yield strength was determined based on the experimental values. The force-displacement results from the analytical model and the experiment are compared in Fig. 6 and it can be observed that the elastic stiffness and therefore the yield displacement are consistent with the experimental data. There are some discrepancies in gap closure or nonlinear transition in unloading branches at larger displacements due to the idealized macromodel. Nevertheless, the analytical model can simulate the behavior of the damper with an acceptable accuracy. It can

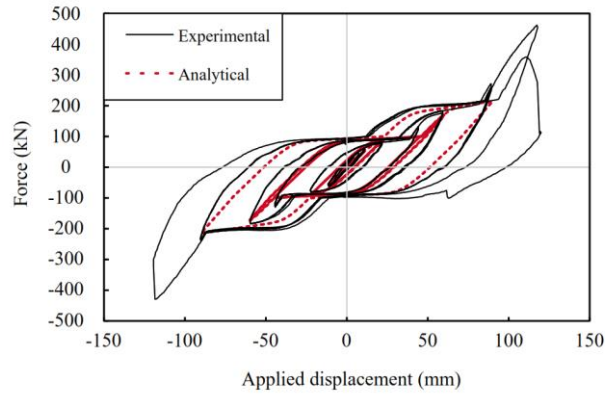


Fig. 6 Comparison of experimental and analytical force-displacement curves of the MSD

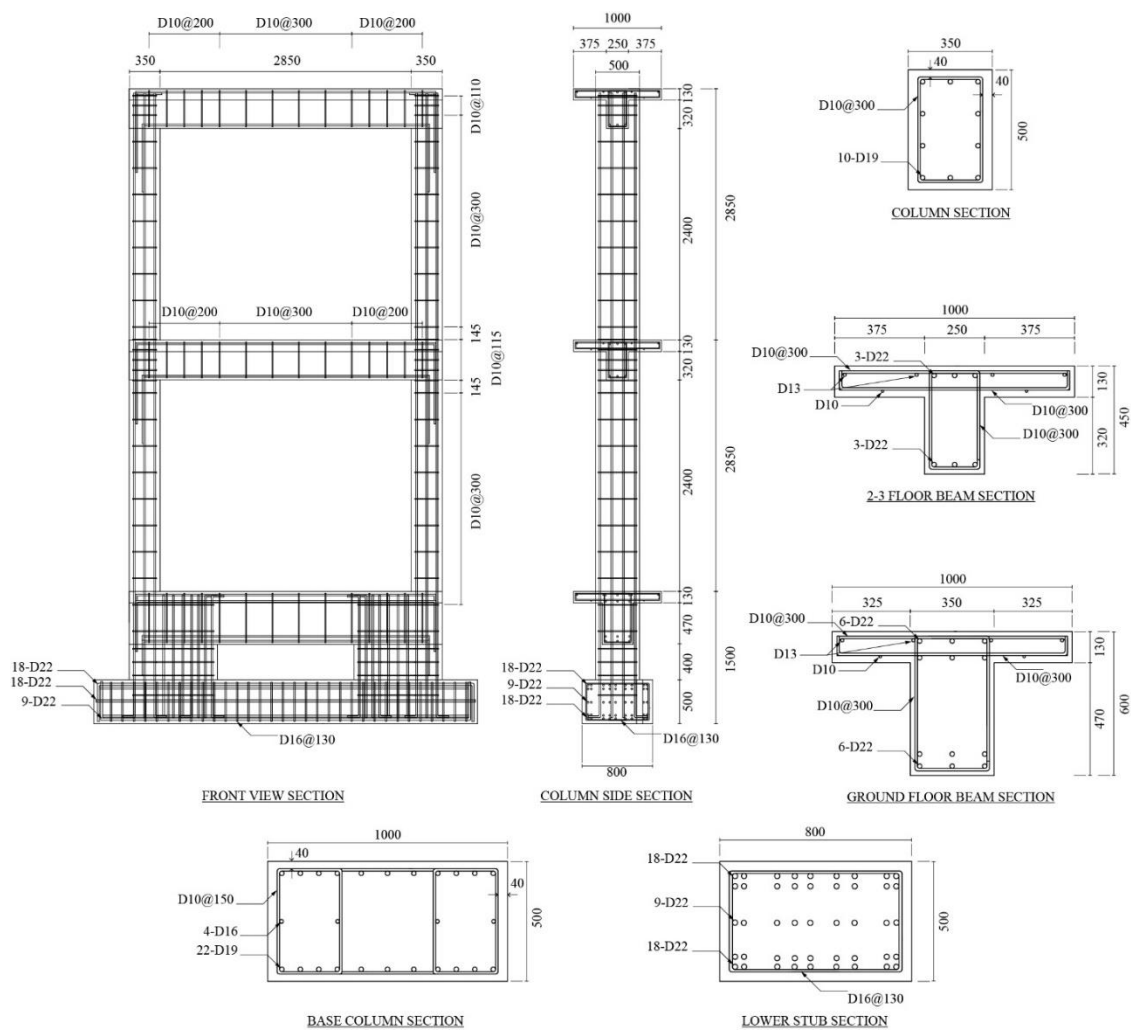


Fig. 7 Details of the two-story RC test frame

be also noticed that the calculated elastic stiffness and the expected yield strengths are in good agreement with the experimental data. Based on this observation, the model was used in the seismic performance evaluation of the 2-story RC frame tests.

3. Experiments of two-story RC frames

In the first part of this section, structural details of the tested RC frame are explained in detail. Next, the test setup and cyclic loading procedure are described followed by the description and discussion of the test results.

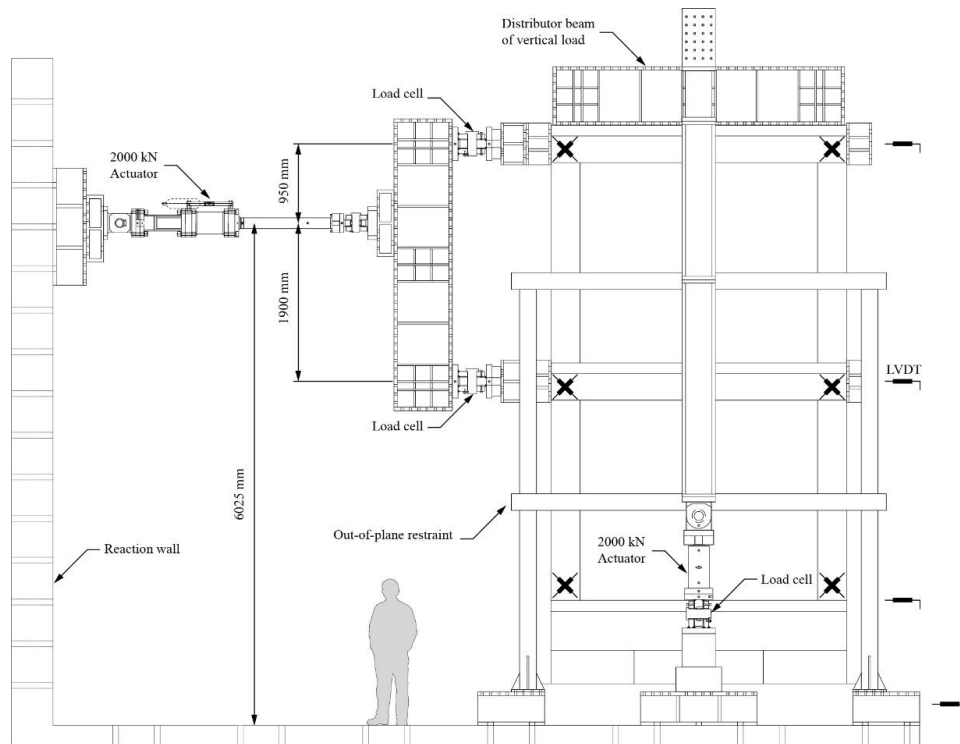


Fig. 8 Details of the test setup and instrumentation

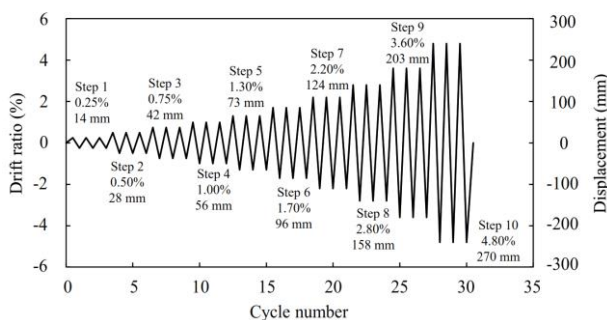


Fig. 9 Loading protocol for the actuator and overall drift ratio of the frame

A two-story RC frame was chosen as a benchmark structure which has dimensions and reinforcement details similar to a typical elementary school built in the 1980s in Korea. The reinforcement details and dimensions of the frame are shown in Fig. 7. In order to provide a fixed-base condition for the frame, a ground floor beam and two base columns were considered which have sections large enough to remain elastic with a negligible deformation during the test. The base columns are over a lower stub which is anchored to the strong floor. The floor-to-floor height of each story is 2850 mm and the length of the bay is 3200 mm. Considering the ground floor beam, base columns, and the lower stub, the overall height of the tested frames is 7200 mm. The yield strength of steel reinforcement obtained from the tensile test is 457 MPa and the 28-day compressive strength of concrete is obtained as 34 MPa.

The seismic performance of the benchmark RC frame was evaluated before and after retrofit using cyclic loading test according to ACI 374 (2005). The details of the test setup and the instrumentation are depicted in Fig. 8. Each story of the frame was subjected to displacement-controlled cyclic load. The displacements were applied in such a way that the corresponding imposed force to the stories followed a triangular load pattern. For this purpose, a distributor member was attached with load cells as shown in Fig. 8, and the actuator applied the displacements to the distributor with the ratio of 1 to 2. The vertical load of 460 kN was applied to the frame using two actuators placed at both sides of the frame, and the force was distributed to the two columns using another distributor placed on the top beam. In addition to the force and the displacement recorded from the actuator, the applied lateral force on each story was recorded using the load cells. Lateral displacement at each story level was measured using linear variable differential transformers (LVDTs) along with the shear deformation and rotations at beam column joints and the base. The displacements of the frame support and slippage at the connection to the strong floor were also observed using LVDTs at the ground floor beam and the lower stub level. As can be seen in Fig. 8, a steel frame was additionally provided to prevent the out-of-plane deformation of the RC frame while applying displacements.

The displacement-controlled cyclic loading was based on the overall drift ratio of the frame. The height of the frame in derivation of the loading protocol was considered from the top of the ground floor beam to the center of the roof beam flange which is 5635 mm. The lateral displacement was measured at the top of the second story.

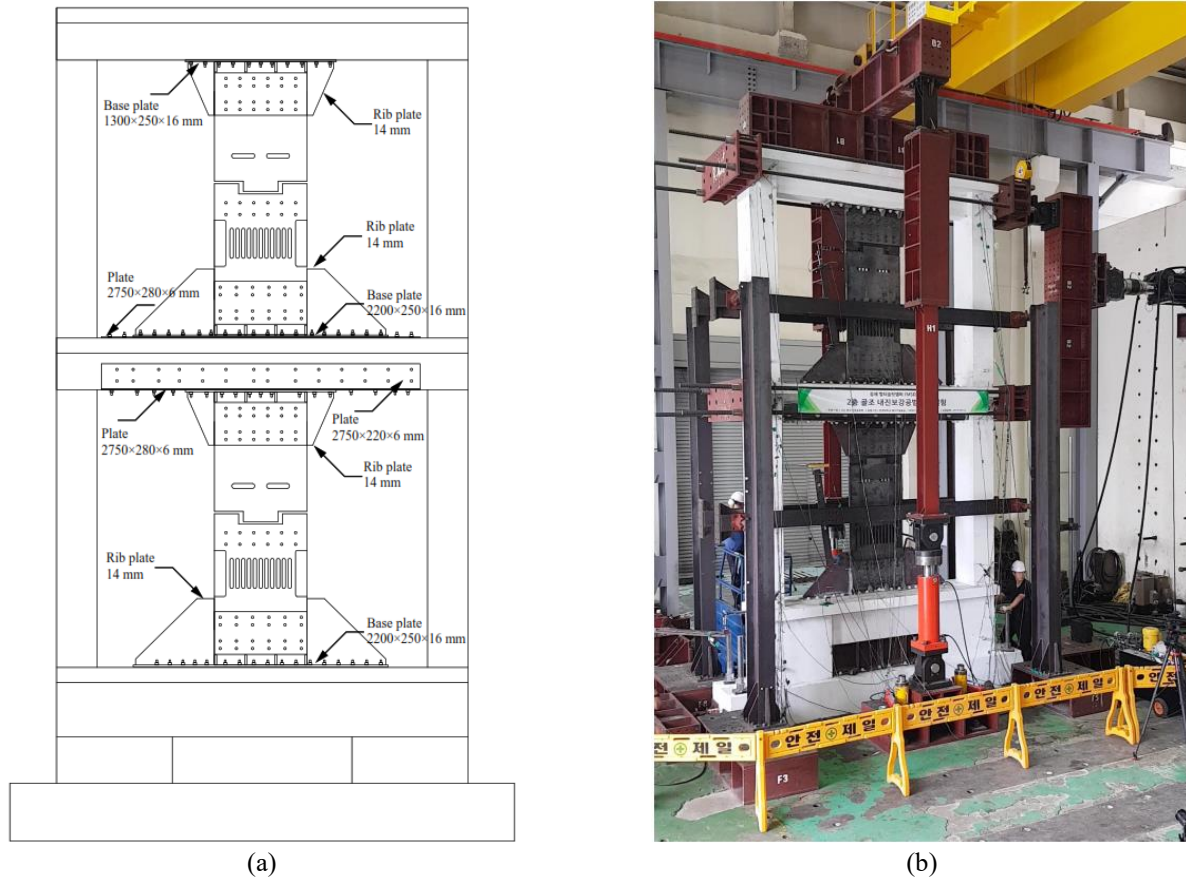


Fig. 10 RC frame retrofitted with MSD-20T: (a) Installation details and (b) test setup

Hence, the displacements were applied so that the recorded top displacement to the frame height follows the predefined loading protocol. The loading protocol is shown in Fig. 9. According to ACI 374, the drift ratio at each step was applied for three cycles. First drift ratio was within the linear elastic range response of the frame and at next steps each drift ratio was considered in such a way that it was not less than 1.25 times and not greater than 1.5 times the drift ratio at the previous step.

The benchmark two-story RC frame was tested under the defined cyclic loading test. Two other frames with identical details and properties were retrofitted with two MSDs with different capacities and were tested under the same conditions. The MSDs were named MSD-20T and MSD-30T which have expected maximum capacities of 200 kN and 300 kN, respectively. The MSDs were made of 15 mm and 20 mm steel plates. The yield strength and ultimate strength of these plates were obtained using steel coupon test and the results are shown in Table 2.

Design, manufacture, and assembly of the MSDs were based on the aforementioned explanations as depicted in Fig. 2. The details and properties of the MSDs are listed in Tables 3 and 4 for MSD-20T and MSD-30T, respectively. Initial yield forces are calculated using given yield strength of steel, however as mentioned before, the maximum capacity is expected to be higher due to the post-yield stiffness and tension field as observed in the damper unit test. Since the strong slit damper of MSD-30T is composed

of two steel plates and each plate has the same dimensions with the weak slit damper, the strong slit damper has a yield force of 247 kN, two times higher than the strength of the weak slit damper. On the other hand, MSD-20T was designed so that the yield forces of its weak and strong slit dampers are 74 kN and 132 kN, respectively. The distance between the weak and strong slit dampers L is 356 mm for both MSD-20T and MSD-30T which is important to calculate the stiffness of the damper.

The test setup of the frame retrofitted with MSD-20T is shown in Fig. 10. The dampers were installed on both stories, and the connections were designed to sustain the shear force and bending moment on the beam. To this end, a base plate with the dimensions of $1300 \times 250 \times 16 \text{ mm}^3$ was installed at the top of the damper using two rows of 11 anchor bolts and a base plate with the dimensions of $2200 \times 250 \times 16 \text{ mm}^3$ at the bottom using two rows of 18 anchor bolts. Since the two dampers were connected to the first story beam, it was reinforced with two $2750 \times 220 \times 6 \text{ mm}^3$ side plates and one $2750 \times 280 \times 6 \text{ mm}^3$ plate at the bottom to prevent premature failure of the beam. Rib plates with a thickness of 14 mm were welded to the base plate and the damper to induce in-plane shear behavior of the damper and to distribute the shear force and bending moments to the base plates evenly. The MSD-30T damper was also installed in another RC frame for the cyclic loading test in the similar manner.

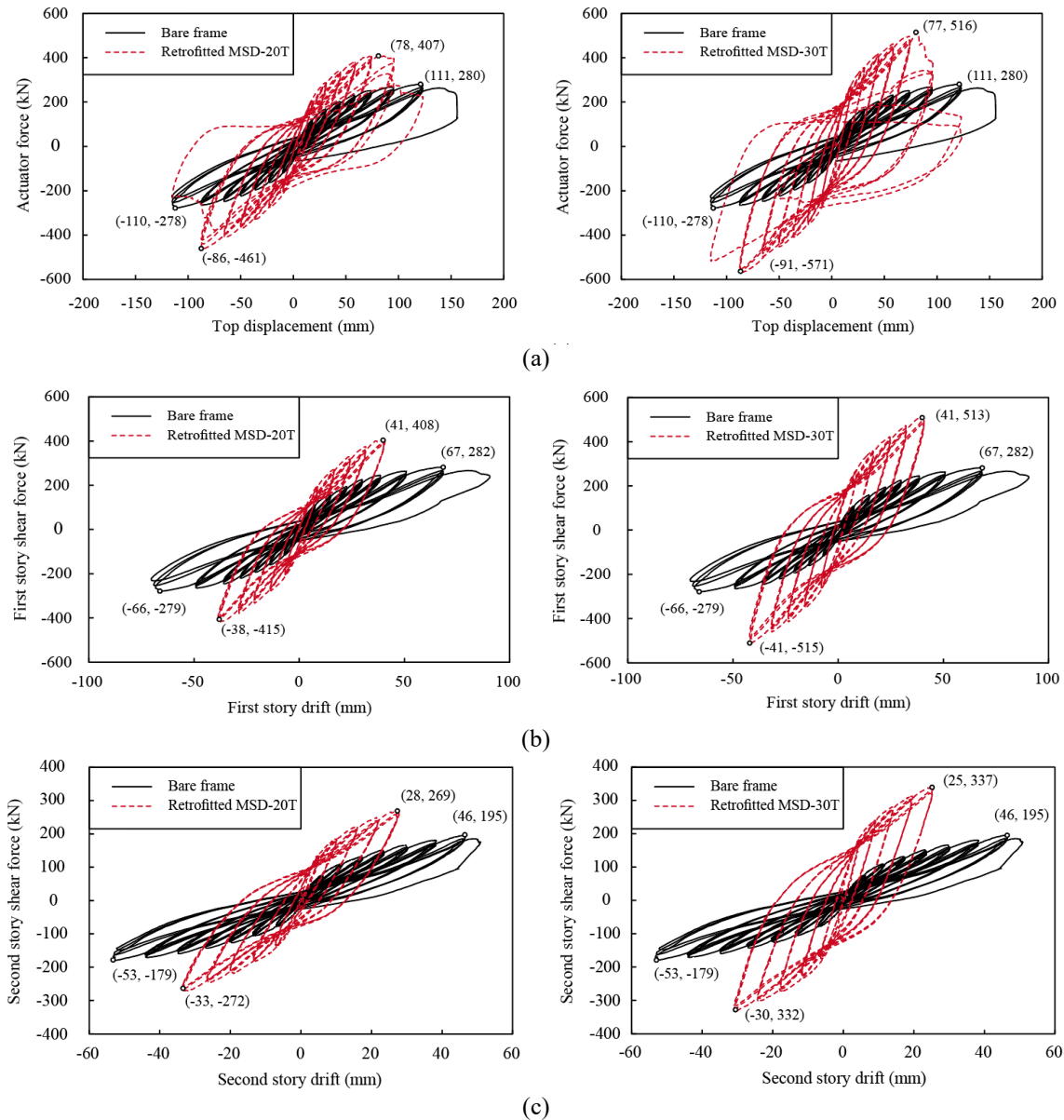


Fig. 11 Results of cyclic loading test of bare and retrofitted frames: (a) Force-top displacement, (b) first story shear force-first story drift and (c) second story shear force-second story drift

Table 2 Average steel coupon test results

Plate thickness (mm)	Yield strength (MPa)	Ultimate strength (MPa)
15	315	353
20	353	403

4. Test results and discussion

The overall behavior of the RC frames including energy dissipation, crack formation, failure mechanism, and plastic hinges before and after the retrofit are investigated based on the data obtained from the actuator, load cells, LVDTs, and strain gauges. The effects of beam reinforcement, modeling method and its accuracy are further evaluated.

4.1 Test results

The overall hysteretic behaviors of the tested RC frames before and after retrofit with MSD-20T and 30T are plotted using the actuator force-top displacement curve as shown in Fig. 11(a). It is observed that the average maximum capacity of the bare frame for the positive and negative directions is 279 kN which corresponds to the overall drift ratio of 2.20% at the 7th step. This capacity is increased to 434 kN and 543 kN for the frames retrofitted with MSD-20T and MSD-30T, respectively. Both forces correspond to the overall drift ratio of 1.3% at the 5th step. The bare frame failed at the first cycle of the 8th step, whereas the retrofitted frames failed at the 6th step. The failure mechanisms, details, and explanations are presented in the next part.

Table 3 Properties of MSD-20T specimen

Damper	Thickness t_i	Slit column length l_i	Slit column width b_j	Gap	Shear stiffness k_s	Rotational stiffness k_θ	Yield force
Weak	20 mm	270 mm	$2 \times 35 \text{ mm} + 8 \times 20 \text{ mm}$	40 mm	$32 \frac{\text{kN}}{\text{mm}}$	$776 \frac{\text{kN.m}}{\text{rad}}$	74 kN
Strong	$2 \times 15 \text{ mm}$	230 mm	$2 \times 35 \text{ mm} + 10 \times 20 \text{ mm}$	40 mm	$86 \frac{\text{kN}}{\text{mm}}$	$1513 \frac{\text{kN.m}}{\text{rad}}$	132 kN



(a)



(b)

Fig. 12 Deformation of MSD-20T: (a) At the end of the 5th cycle and (b) at the end of the 7th cycle

Table 4 Properties of MSD-30T specimen

Damper	Thickness t_i	Slit column length l_i	Slit column width b_j	Gap	Shear stiffness k_s	Rotational stiffness k_θ	Yield force
Weak	20 mm	250 mm	$14 \times 25 \text{ mm}$	40 mm	$59 \frac{\text{kN}}{\text{mm}}$	$1225 \frac{\text{kN.m}}{\text{rad}}$	123 kN
Strong	$2 \times 20 \text{ mm}$	250 mm	$14 \times 25 \text{ mm}$	40 mm	$118 \frac{\text{kN}}{\text{mm}}$	$2450 \frac{\text{kN.m}}{\text{rad}}$	247 kN

The hysteresis behavior of each story was investigated separately using its shear force and interstory drift. The shear forces were obtained using the load cells on each story and the interstory drift was calculated using the LVDT displacements recorded at each story level. The shear force of the second story is equal to the force recorded from the load cell attached to the second story and the shear force of the first story is the sum of the forces recorded from the load cells at the first and second stories, or the actuator force. The interstory drift of the first story is obtained by subtracting the ground floor displacement from the first story displacement. Similarly, the difference between the

second and first story displacements gives the interstory drift of the second story.

The behavior of the first and the second stories is shown in Figs. 11(b) and 11(c), respectively. Although the cyclic loading test of the retrofitted frames was continued till the end of the 7th step, the results are shown for 5 steps due to the shear failure of the column at the ground floor at the onset of the 6th step and subsequent removal of the LVDT.

The average maximum shear forces of the first story are 280 kN, 411 kN, and 514 kN for the bare frame and the frames retrofitted with MSD-20T and MSD-30T, respectively.

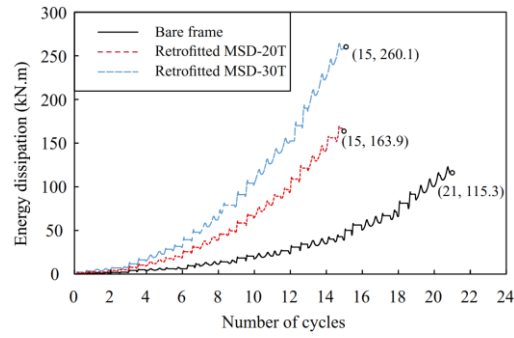


Fig. 13 Cumulative energy dissipation of tested RC frames

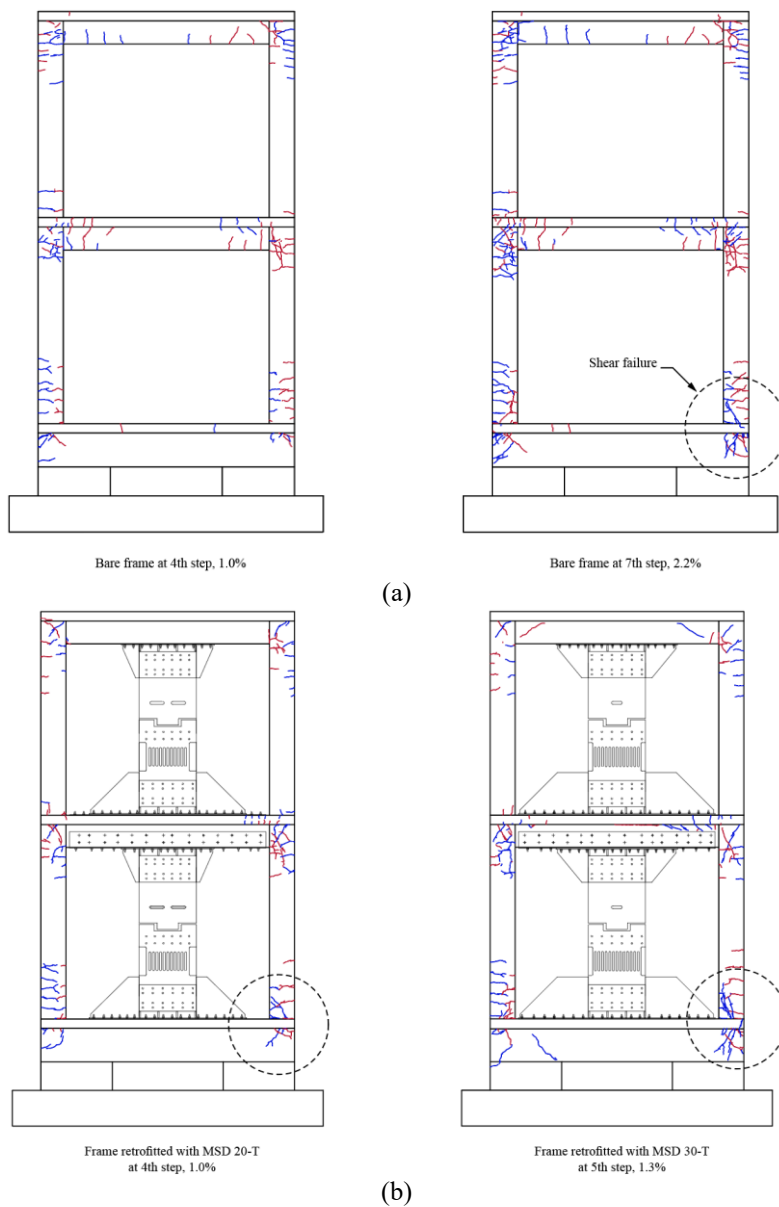


Fig. 14 Crack formation of tested RC frames: (a) Bare frame; (b) retrofitted frames

These forces are related to the interstory drifts of 66 mm, 39 mm, and 41 mm, respectively, which are averaged in the positive and negative directions. Similarly, the

maximum second story shear forces are respectively 187 kN, 270 kN, and 334 kN for the bare frame, and the frames retrofitted with MSD-20T and MSD-30T which

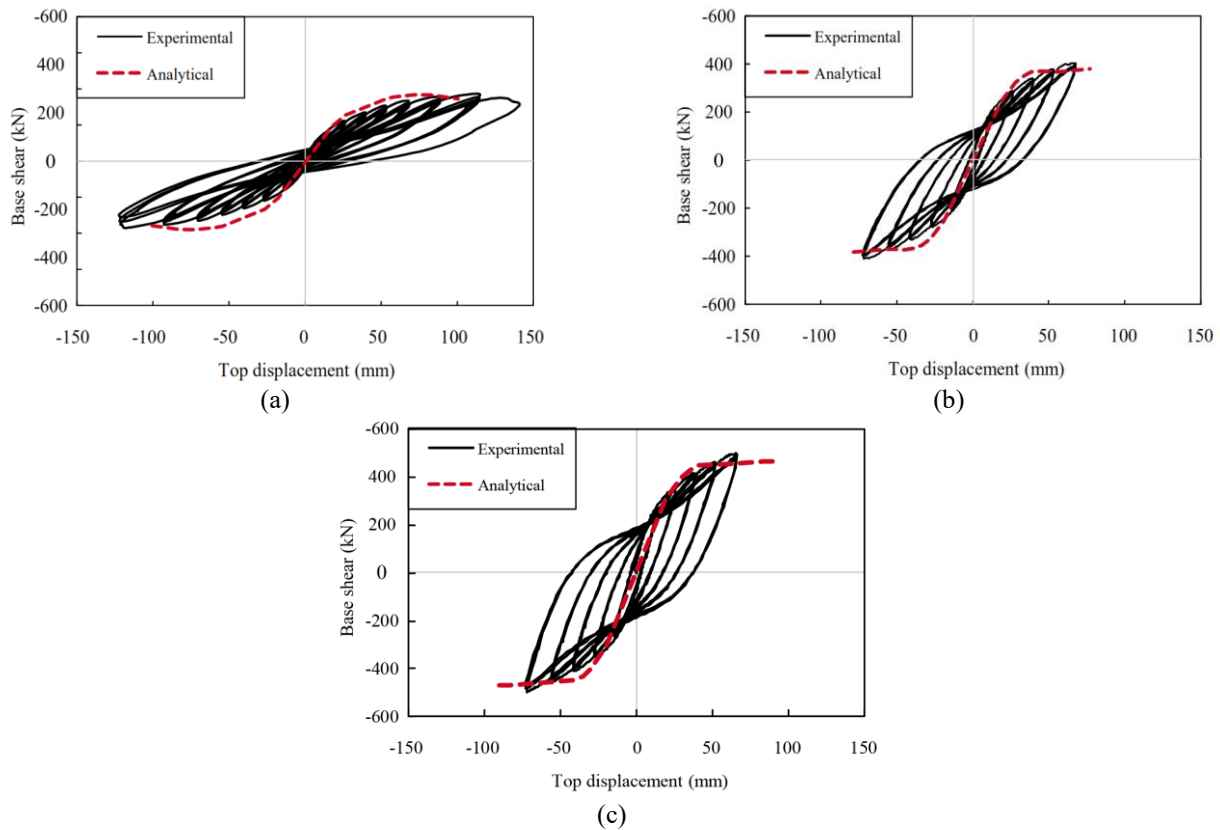


Fig. 15 Comparison of pushover curves and the envelope of experimental hysteresis curves: (a) Bare frame, (b) frame retrofitted with MSD-20T and (c) frame retrofitted with MSD-30T

correspond to the interstory drifts of 49 mm, 30 mm, and 27 mm.

It is seen that the maximum strength of each story was increased with respect to the strength of the applied damper. The interstory drifts were smaller than the 40 mm gap of the MSDs, and therefore the strong slit dampers were not activated before the failure. The MSD at the end of the 5th step is shown in Fig. 12(a) and it is seen that the gap was about to close. The deformation of MSD-20T at the end of the 7th cycle is shown in Fig. 12(b), and it can be seen that the strong slit damper was activated.

The cumulative energy dissipations of the bare and retrofitted frames were calculated using the actuator force-displacement (Fig. 13). The cumulative energy dissipations of the frames retrofitted with MSD-20T and MSD-30T were respectively increased by 42% and 126% after the retrofit, although they failed in smaller displacement.

The cracks were marked on the RC frames at each loading step to identify the damage extent, performance of the structures, and failure mechanisms. The crack formation figures were provided by drawing cracks at the end of each step using high-resolution photos taken from the RC frames. These figures are shown in Fig. 14 for the bare frame at the overall drift ratios of 1.0% and 2.2% and for the frames retrofitted with MSD-20T and MSD-30T at 1.0% and 1.3%, respectively. These drift ratios correspond to the 4th step and the final steps prior to the drastic drop in the strength.

As observed in Fig. 14, the failure mechanism of all tested RC frames was due to the flexural-shear failure of the first story column connected to the ground floor beam. There is no much difference between the crack patterns of the retrofitted frames especially at 1.0%. Flexural cracks of columns are propagated in the horizontal direction whereas the diagonal cracks are due to the shear. It is observed that the shear cracks leading to the final failure were formed in the retrofitted frame at 1.0% drift ratio, while only the flexural cracks are visible in the bare frame at this stage. The main reason for this phenomenon and reduction in ductility is the reinforcement of the beams in the retrofitted structures which leads to concentration of damage in the columns.

In general, cracks show more damage in the first story in both bare and retrofitted frames due to the larger shear force and drift. Accordingly, the cracks of the second story columns are limited to flexural cracks in both bare and retrofitted frames. The connections of the dampers remained in a good condition and no failure was observed. Due to the application of the damper, some shear cracks are visible at the ground floor beam and the second story beam of the retrofitted frames which were not reinforced. Nevertheless, the visible cracks also show that the beam reinforcement and the designed connections performed well, while large bending moment and shear force were imposed on the beams by the dampers.

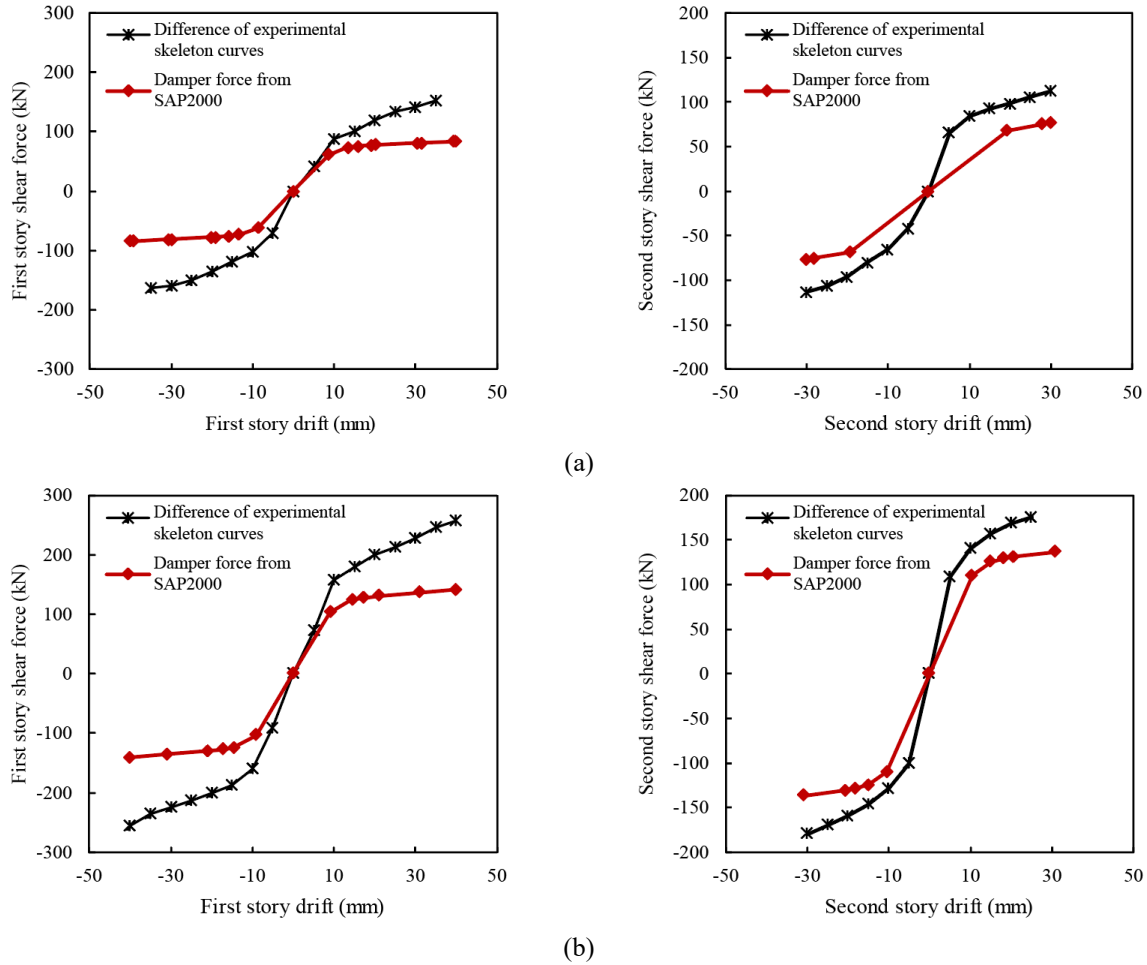


Fig. 16 Investigation of beam reinforcement effects on each story using the damper force and the difference between experimental skeleton curves of shear force-drift before and after the retrofit: (a) Frame retrofitted with MSD-20T, (b) frame retrofitted with MSD-30T

4.2 Pushover analysis of the RC frames

The analysis model of the test specimens was established to further investigate the seismic behavior of the specimens. The analysis model was developed in *SAP2000* using the test data and the details of the bare frame. The dampers for the retrofitted cases were modeled using the elaborated analytical and theoretical formulation provided in Section 2 and details of the damper in Table 3 and 4. The elastic modulus of concrete was obtained equal to 2.7×10^4 MPa based on ACI 318M-14 (ACI 2014) as

$$E_c = 4700\sqrt{f'_c} \quad (9)$$

where f'_c is the specified concrete strength. The effects of rebar confinement was taken into account using the model of Mander *et al.* (1988). The elastic modulus of steel was assumed to be 2.0×10^5 MPa. The nonlinearity of beam-column elements was modeled using lumped plastic hinges according to ASCE 41-13 (2013).

Nonlinear static pushover analyses of the RC frames were carried out in *SAP2000* using the same loading conditions and the pushover curves were compared with the

envelop curves obtained from the tests in Fig. 15. It is seen that the analysis models of both RC frames and dampers can sufficiently account for the nonlinear behavior of the test specimens.

The effects of beam reinforcement for each story were evaluated by comparing the damper force and the difference between skeleton curves of story shear force-drift before and after the retrofit. The damper force was determined using the validated analysis model of the damper, and the difference in skeleton curves on each story was obtained from the experimental data. The results are demonstrated in Fig. 16. It is observed that, in addition to the strength provided by the damper, there is an extra resistance on each story due to the beam reinforcement with the steel plates. This reinforcement includes the base plate and side plates anchored to the beams and the welded rib plates. By averaging in the positive and negative directions, these effects up to the point shown in the figure are respectively 75 kN and 36 kN in the first and second stories of the frame retrofitted with MSD-20T, and 115 kN and 39 kN in the frame retrofitted with MSD-30T.

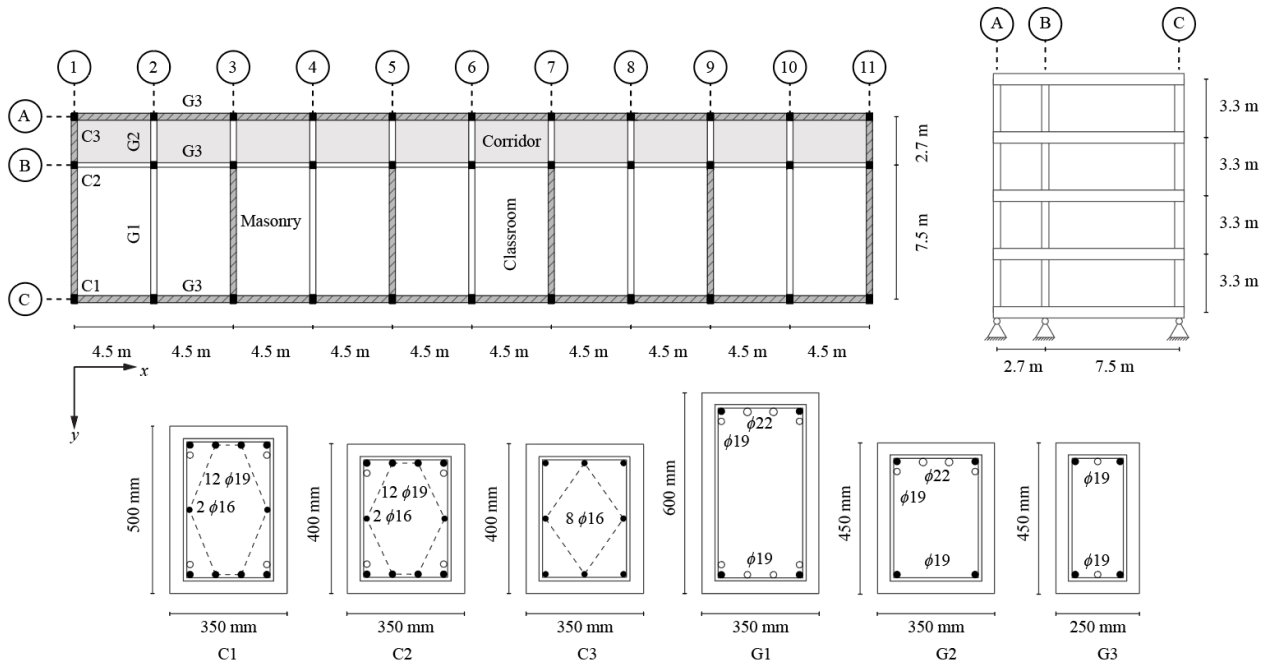


Fig. 17 Details of school building

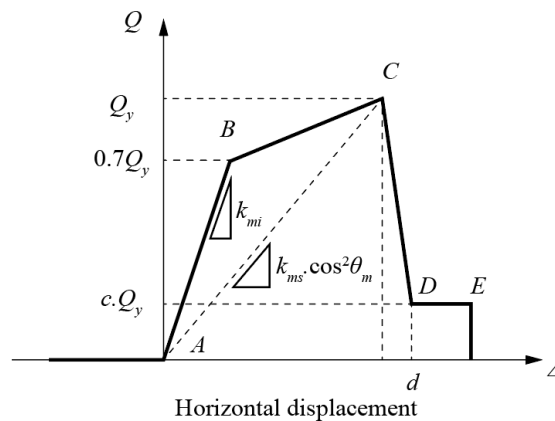


Fig. 18 Backbone curve of masonry infills

5. Application to a case study structure

5.1 Seismic performance of the structure

In order to evaluate the efficiency and applicability of the proposed retrofit scheme, a school building built in the 1980s without considering seismic load was chosen as the case study structure. The plan layout of structure and sectional properties are shown in Fig. 17. Except for the roof, each floor is divided into corridor and classroom. The masonry walls are located between each classroom, and there are short masonry walls below the windows.

The nominal compressive strength of concrete is 18 MPa and the yield strength of steel is 240 MPa. The elastic modulus of concrete used in the analysis model is obtained to be 1.9×10^4 MPa using Eq. (9). The expected compressive strength of concrete and the expected yield

strength of steel were determined respectively by the factors of 1.2 and 1.25 according to the building code of Korea.

The masonry infills were modeled as equivalent compressive struts. The height h_m of the masonry infill walls located between each classroom is 2850 mm, and the height of the masonry walls below the windows in the x-direction is 800 mm. The backbone curve of the struts was obtained in accordance with the Korean seismic code as depicted in Fig. 18 for the horizontal component of the infill. It was assumed that the masonry has a poor condition with the compressive strength f'_m of 2.1 MPa and shear strength f_{vi} of 0.09 MPa.

The analysis model of the structure was established in *SAP2000* considering all requirements of ASCE 41-13. Based on the modal analysis, the fundamental period of the structure was 0.83 s with the predominant response in the x-direction. The seismic performance of the structure was

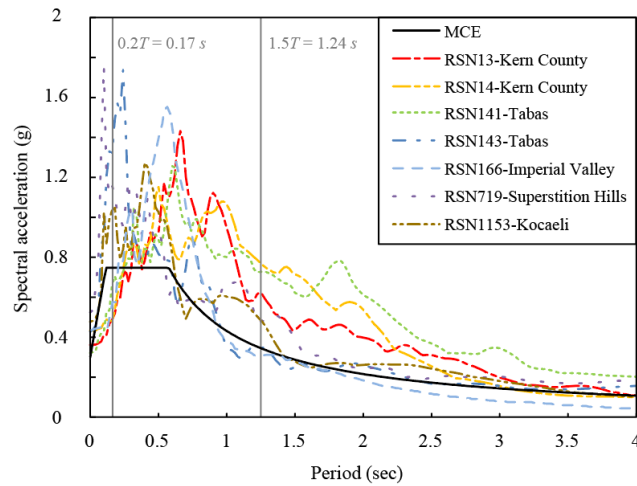


Fig. 19 Response spectra for seven scaled earthquake ground motion records and MCE level design spectrum

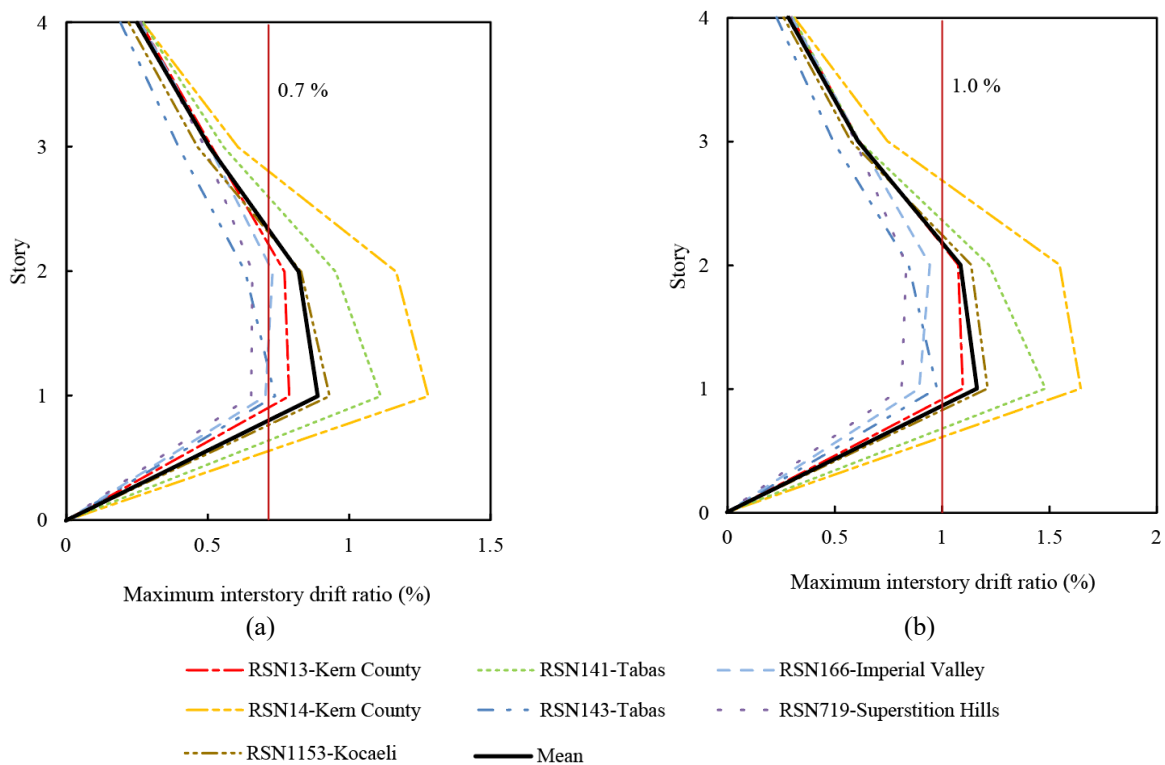


Fig. 20 Seismic performance of the case study building in terms of maximum interstory drift ratios: (a) DBE level and (b) MCE level

assessed in detail using nonlinear time history analysis and seven earthquake ground motions. According to the Korea seismic retrofit guidelines for school buildings, the seismic performance of school buildings should satisfy limit states for both 1.2 times the design basis earthquake (DBE) and the maximum considered earthquake (MCE). For this purpose, seven far field earthquake records were chosen from the PEER NGA database (2014), and were scaled to the target response spectra in accordance with the Korean seismic code in such a way that the average square root of the sum of the squares (SRSS) of the record pairs does not

fall below 1.3 times the target spectrum in the period range of $0.2T$ and $1.5T$ where T is the fundamental period of the structure. The structure is assumed to be located on site class S_D which has the average shear wave velocity between 180 m/s and 360 m/s on the upper 30 m of the subsoil. The response spectra of the seven earthquake ground motion records along with the target spectrum for the MCE level are depicted in Fig. 19.

The seismic performance of the structure for the considered two earthquake hazards is shown in Fig. 20. The mean values of the maximum interstory drift ratios are

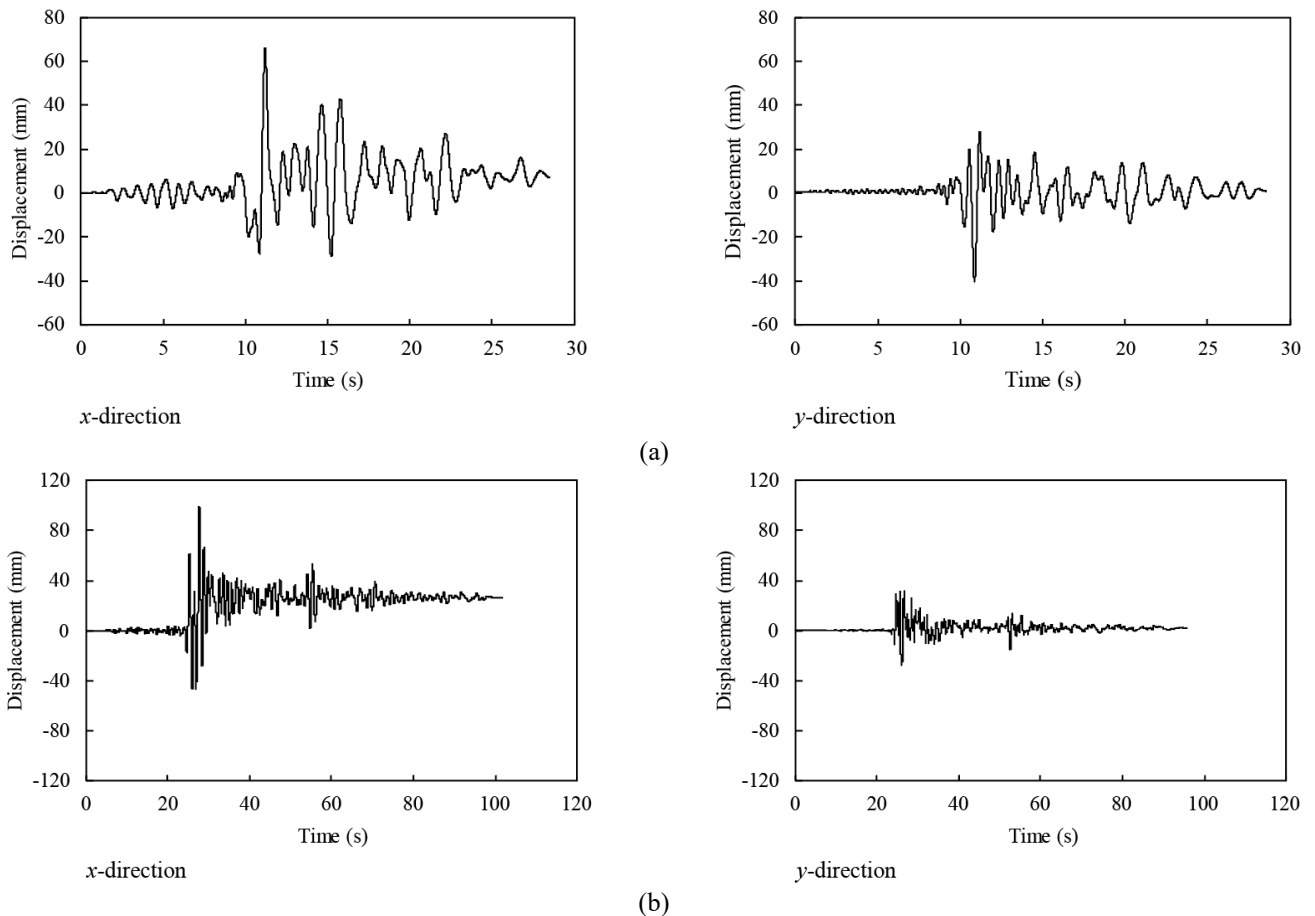


Fig. 21 Roof displacement time history: (a) RSN14-Kern County earthquake (DBE) and (b) RSN1153-Kocaeli earthquake (MCE)

0.9% and 1.2% for the DBE and MCE levels, respectively, which occur in the first story. The maximum interstory drift ratios of different stories are between 0.2% and 1.3% for the DBE and 0.2% and 1.6% for the MCE level earthquakes. Based on the guidelines, the structure modeled with masonry infills shall meet 0.7% and 1.2% maximum interstory drift ratios for the DBE and MCE levels, respectively. As the structural response exceeds the required limit states, seismic retrofit is required.

The roof displacement time histories under the RSN14-Kern County and RSN1153-Kocaeli earthquake ground motion records are shown in Fig. 21 for the DBE and MCE levels, respectively. It is observed that the maximum and the residual displacements of the structure in the x-direction are much larger than those in the y-direction in which story-high masonry infill walls are located.

5.2 Seismic retrofit of the case study structure

According to the results of nonlinear time history analysis, the structure needs to be retrofitted in the x-direction. To estimate the required number of dampers, the capacity spectrum method presented in ATC 40 (1996) was used. The bilinear capacity spectrum of the structure was obtained using the pushover curve in the x-direction and drawn against the 5% elastic demand spectra for the

DBE and MCE levels. In addition to the 5% inherent damping, the structure has hysteretic damping due to nonlinear deformation. This damping ratio is denoted by $\kappa\beta_0$, where κ accounts for imperfections in hysteresis loops and degradation. The elastic demand spectrum is reduced based on the effective damping ratio β_{eff} which is the sum of the aforementioned damping sources and energy dissipation devices.

The school building structure was assumed to have structural behavior type C according to ATC-40, indicating that the structure consists of noncomplying primary elements with poor or unreliable hysteretic behavior. The performance point d_p before retrofit was calculated so that the effective damping ratio of the structure at point $\beta_{eff} = 5\% + \kappa\beta_0$ is equal to the damping ratio of the reduced spectrum intersecting the capacity spectrum. The procedure and detailed results are shown in Fig. 22. The target performance points d_p are 104 mm and 149 mm for the DBE and MCE levels respectively, which correspond to the maximum interstory drift ratios of 1.3% and 1.9% based on the modal participation factor of $\Gamma = 1.247$ and the mode shape vector of $\phi^T = [0.34, 0.64, 0.87, 1.0]$.

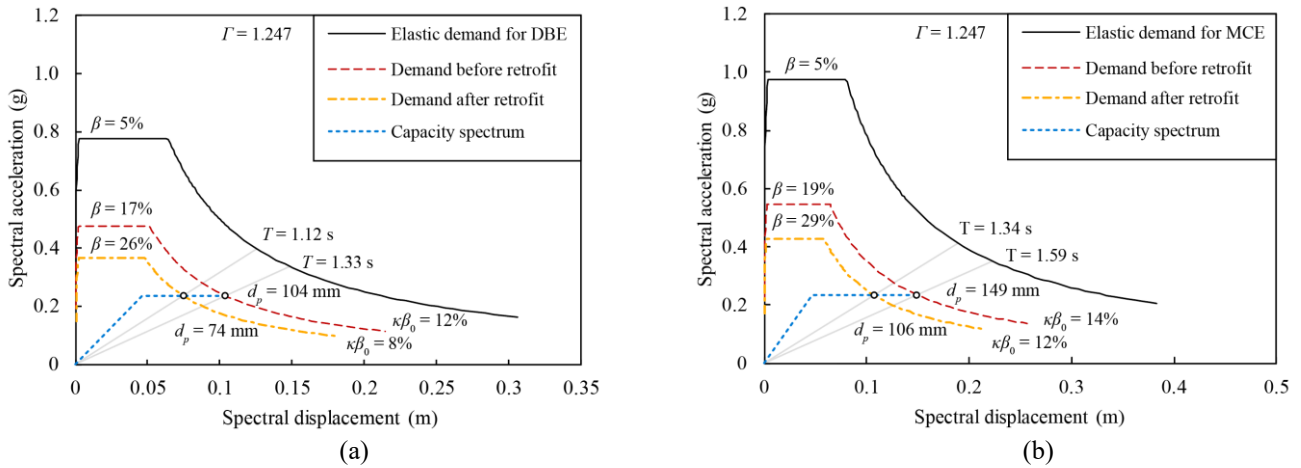


Fig. 22 Estimation of the performance point before retrofit and required damping ratio to satisfy limit states: (a) DBE level and (b) MCE level

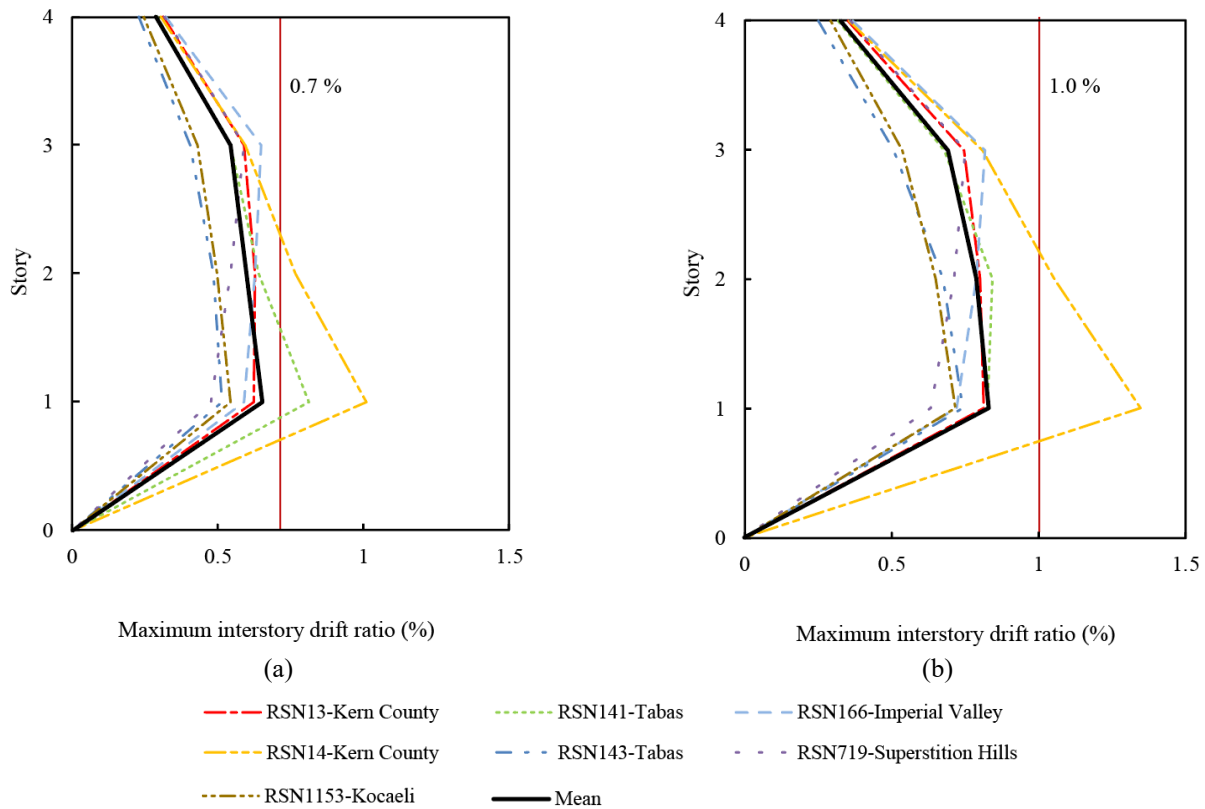


Fig. 23 Seismic performance of the school building structure after retrofit in terms of maximum interstory drift ratios under seven earthquakes: (a) DBE level and (b) MCE level

To retrofit the structure, the capacity spectrum method was used for the preliminary estimate of the required number of dampers, and the seismic performance of the retrofitted structure was further evaluated using nonlinear time history analysis. To obtain the required effective damping to meet the limit states, the performance points d_p for the DBE and MCE levels were calculated so that the average maximum interstory drift ratios on each story are

respectively 0.7% and 1%. Considering the story height of 3.3 m and the modal participation factor, these drift ratios correspond to the performance points of 74 mm and 106 mm for the DBE and MCE levels, respectively. The provided damping ratio by the structure $5\% + \kappa\beta_0$ for these performance points are 13% and 17% whereas the required effective damping ratio β_{eff} to meet these limit states are 26% and 29%. The demand spectrum after retrofit is also depicted in Fig. 22.

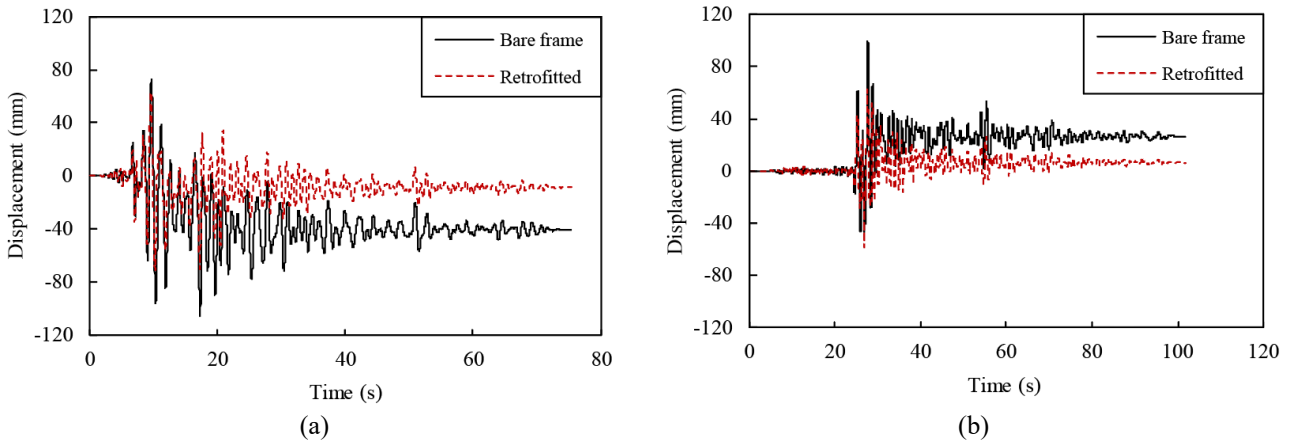


Fig. 24 Roof displacement time history in x-direction: (a) RSN14-Kern County earthquake (DBE) and (b) RSN1153-Kocaeli earthquake (MCE)

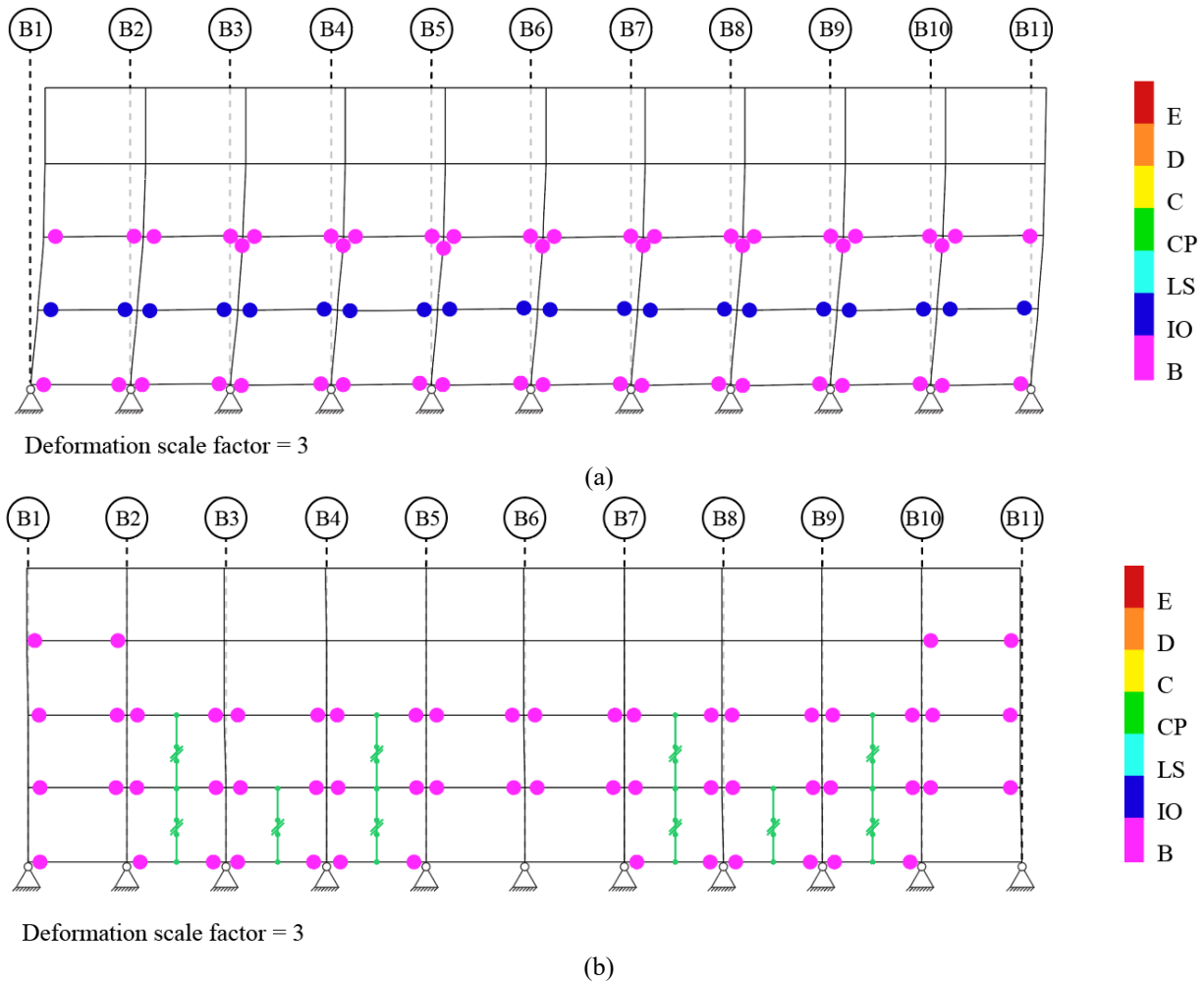


Fig. 25 Plastic hinge formation under the RSN1153-Kocaeli earthquake (MCE): (a) Before retrofit and (b) after retrofit

The remaining damping was provided by the dampers and calculated according to ASCE 41-13 using

$$\beta_{eff} = 5\% + \kappa\beta_0 + \frac{\sum_j W_j}{4\pi W_k} \quad (10)$$

where W_j is the work done by the j th damper in one complete cycle which is equal to the area inside the hysteresis curve. W_k is the maximum strain energy which is the potential energy stored in the structure at the performance point determined as

$$W_k = \frac{1}{2} \sum_i F_i \delta_i \quad (11)$$

where F_i is the imposed lateral load at the i th reactive weight and δ_i is the corresponding displacement.

By using the aforementioned estimation procedure, hysteresis curve of the damper, pushover curve, fundamental mode shape, and the available locations in the plan layout, the number of required dampers was estimated. It was found that 6 MSD-30T dampers on the first story, 6 on the second story, and 4 on the third story was enough for the DBE level. The same retrofit scheme was acceptable for the MCE level, except for the second story where 4 dampers could be installed. As a rough estimate using the capacity spectrum method, it was decided to try 6 dampers on the first story and 4 on the second story due to the smaller drifts on upper stories. For validation of the retrofit design, the seismic performance of the structure after the retrofit strategy was evaluated using nonlinear time history analysis.

The maximum interstory drift ratios of the retrofitted structure obtained from nonlinear dynamic analysis using the seven earthquake records are depicted in Fig. 23, where it can be observed that the mean maximum interstory drift ratios, 0.6% and 0.8% for the DBE and MCE levels, respectively, meet the target limit states. The maximum interstory drift ratios in all stories are between 0.2% and 1.0% for the DBE and 0.2% and 1.3% for the MCE.

The roof displacement time histories of the structure subjected to the DBE level RSN14-Kern County and the MCE level RSN1153-Kocaeli earthquakes are demonstrated for the x-direction in Fig. 24. It can be observed that both maximum and residual displacements were reduced after the retrofit. Fig. 25 depicts the plastic hinge formation in the structure subjected to the RSN1153-Kocaeli earthquake (MCE), where it is observed that the rotation of the beam plastic hinges was reduced and no plastic hinges formed in the columns of the retrofitted frame, whereas the columns in the second story of the bare frame were damaged.

5. Conclusions

This research investigated a seismic retrofit scheme using a steel plate multi-slit damper. Two-story RC frames with and without seismic retrofit were tested under cyclic loading; one bare frame and two frames retrofitted with multi-slit dampers with expected maximum capacities of around 200 kN and 300 kN were tested. The analytical model of the damper was derived and was used to simulate the test results. The developed damper was applied to seismic retrofit of a four-story case study RC building structure. The seismic performance of the structure was evaluated before and after retrofit in terms of the maximum strength, maximum inter-story drift ratio, residual displacement, deformations of the structure, and plastic hinge formation.

The cyclic loading test results showed that the average maximum capacity of the bare frame was 279 kN, which was increased to 434 kN and 543 kN in the frames

retrofitted with MSD-20T and MSD-30T, respectively. The nonlinear dynamic analysis of the case study structure under seven earthquake ground motions showed that the mean values of the maximum inter-story drift ratios were 0.9% and 1.2% for the DBE and MCE levels, respectively, which exceeded the limit states of 0.7% and 1.0%, respectively. The analysis of the model structure retrofitted with the multi-slit dampers showed that the mean maximum inter-story drift ratios were reduced to 0.6% and 0.8% for the DBE and MCE levels, respectively, which met the target limit states. The test and analysis results showed that the developed retrofit scheme could be effective in improving the seismic performance of framed structures.

Acknowledgments

This research was carried out by research funding (task number 21CTAP-C152050-03) of the Ministry of Land, Infrastructure and Transport, Land Transport Technology Promotion Research Project.

References

- ACI. (2005), Acceptance Criteria for Moment Frames Based on Structural Testing and Commentary (ACI 374.1-05). American Concrete Institute, Farmington Hills, MI.
- ACI (American Concrete Institute). (2014), Building Code Requirements for Structural Concrete (ACI 318M-14) and Commentary (ACI 318RM-14). American Concrete Institute (ACI), Farmington Hills, MI.
- ASCE. (2013), Seismic rehabilitation of existing buildings. ASCE/SEI 41-13, ASCE, Reston, VA.
- ATC. (1996), Seismic Evaluation and Retrofit of Concrete Buildings. Applied Technology Council, Redwood City, CA.
- Bahrani, M.K., Nooralizadeh, A., Usefi, N. and Zargarani, M. (2019), "Seismic evaluation and partial retrofitting of concrete bridge bents with defect details", *Latin American Journal of Solids and Structures, Brazilian Association of Computational Mechanics*, **16**(8). <https://doi.org/10.1590/1679-78255158>.
- Chan, R.W.K. and Albermani, F. (2008), "Experimental study of steel slit damper for passive energy dissipation", *Eng. Struct.*, **30**(4), 1058-1066. <https://doi.org/10.1016/j.engstruct.2007.07.005>.
- Choi, H. and Kim, J. (2010). "New installation scheme for viscoelastic dampers using cables", *Can. J. Civil Eng.*, **37**(9), 1201-1211. <https://doi.org/10.1139/L10-068>.
- Computers and Structures Inc. (CSI). (2017), "SAP2000." Berkeley, CA.
- Javidan, M.M., Kang, H., Isobe, D. and Kim, J. (2018), "Computationally efficient framework for probabilistic collapse analysis of structures under extreme actions", *Eng. Struct.*, **172**, 440-452. <https://doi.org/10.1016/j.engstruct.2018.06.022>.
- Javidan, M.M. and Kim, J. (2019a), "Seismic retrofit of soft-first story structures using rotational friction dampers", *J. Struct. Eng.*, **145**(12), 04019162. [https://doi.org/10.1061/\(ASCE\)ST.1943-541X.0002433](https://doi.org/10.1061/(ASCE)ST.1943-541X.0002433).
- Javidan, M.M. and Kim, J. (2019b), "Variance-based global sensitivity analysis for fuzzy random structural systems", *Comput. - Aided Civil Infrastruct. Eng.*, **34**(7). <https://doi.org/10.1111/mice.12436>.
- Javidan, M.M. and Kim, J. (2020a), "Experimental and Numerical Sensitivity Assessment of Viscoelasticity for Polymer

- Composite Materials”, *Scientific Reports, Nature Research*, **10**(1), 1-9. <https://doi.org/10.1038/s41598-020-57552-3>.
- Javidan, M.M. and Kim, J. (2020b), “Steel hysteretic column dampers for seismic retrofit of soft-first-story structures”, *Steel Compos. Struct.*, **37**(3), 259–272. <http://dx.doi.org/10.12989/scs.2020.37.3.259>.
- Kim, J. and Bang, S. (2002), “Optimum distribution of added viscoelastic dampers for mitigation of torsional responses of plan-wise asymmetric structures”, *Eng. Struct.*, **24**(10), 1257–1269. [https://doi.org/10.1016/S0141-0296\(02\)00046-9](https://doi.org/10.1016/S0141-0296(02)00046-9).
- Kim, J., Choi, H. and Chung, L. (2004), “Energy-based seismic design of structures with buckling-restrained braces”, *Steel Compos. Struct.*, **4**(6), 437–452. <https://doi.org/10.12989/scs.2004.4.6.437>.
- Kim, J., Park, J. and Kim, S.D. (2009), “Seismic behavior factors of buckling-restrained braced frames”, *Struct. Eng. Mech.*, **33**(3), 261–284. <https://doi.org/10.12989/sem.2009.33.3.261>.
- Kim, J. (2019), “Development of seismic retrofit devices for building structures”, *Int. J. High-Rise Build.*, **8**(3), 221–227. <https://doi.org/10.21022/IJHRB.2019.8.3.221>.
- Lee, J. and Kim, J. (2015), “Seismic performance evaluation of moment frames with slit-friction hybrid dampers”, *Earthq. Struct.*, **9**(6), 1291–1311. <http://dx.doi.org/10.12989/eas.2015.9.6.1291>.
- Lee, J. and Kim, J. (2017), “Development of Steel Box-shaped slit dampers for Seismic Retrofit of building structures”. *Eng. Struct.*, **150**, 934–946. <https://doi.org/10.1016/j.engstruct.2017.07.082>.
- Lee, S.K., Park, J.H., Moon, B.W., Min, K.W., Lee, S.H. and Kim, J. (2008), “Design of a bracing-friction damper system for seismic retrofiting”, *Smart Struct. Syst.*, 685–696. <https://doi.org/10.12989/sss.2008.4.5.685>.
- Mander, J.B., Priestley, M.J.N. and Park, R. (1988), “Theoretical Stress-Strain Model for Confined Concrete”, *J. Struct. Eng.*, **114**(8), 1804–1826. [https://doi.org/10.1061/\(ASCE\)0733-9445\(1988\)114:8\(1804\)](https://doi.org/10.1061/(ASCE)0733-9445(1988)114:8(1804)).
- Mohammadi, M., Kafi, M.A., Kheyroddin, A. and Ronagh, H.R. (2020a), “Performance of innovative composite buckling-restrained fuse for concentrically braced frames under cyclic loading”, *Steel Compos. Struct.*, **36**(2), 163–177. <http://dx.doi.org/10.12989/scs.2020.36.2.163>.
- Mohammadi, M., Kafi, M.A., Kheyroddin, A., Ronagh, H.R. and Rashidi, M. (2020b), “Experimental and Numerical Investigation of Innovative Composite Buckling-Restrained Fuse”, *Lecture Notes in Civil Engineering*, 113–121. https://doi.org/10.1007/978-981-13-7603-0_12.
- Naeem, A. and Kim, J. (2019), “Seismic performance evaluation of a multi-slit damper”, *Eng. Struct.*, **189**, 332–346. <https://doi.org/10.1016/j.engstruct.2019.03.107>.
- Noureldin, M., Kim, J. and Kim, J. (2018), “Optimum distribution of steel slit-friction hybrid dampers based on life cycle cost”, *Steel Compos. Struct.*, **27**(5), 633–646. <http://dx.doi.org/10.12989/scs.2018.27.5.633>.
- Park, J., Lee, J. and Kim, J. (2012), “Cyclic test of buckling restrained braces composed of square steel rods and steel tube”, *Steel Compos. Struct.*, **13**(5), 423–436. <https://doi.org/10.12989/scs.2012.13.5.423>.
- PEER. (2014), “PEER NGA Database.” PEER Ground Motion Database, <<https://ngawest2.berkeley.edu/>>.
- Saffari, H., Hedayatb, A.A. and Poorsadeghi, N.M. (2013), “Post-Northridge connections with slit dampers to enhance strength and ductility”, *J. Constr. Steel Res.*, **80**(1), 138–152. <https://doi.org/10.1016/j.jcsr.2012.09.023>.
- Shin, J., Lee, K., Jeong, S.H., Lee, H.S. and Kim, J. (2012), “Experimental and analytical studies on Buckling-Restrained Knee Bracing systems with channel sections”, *Int. J. Steel Struct.*, **12**(1), 93–106. <https://doi.org/10.1007/s13296-012-1009-Y>.
- Usefi, N., Ronagh, H., Kildashti, K. and Samali, B. (2018), “Macro/micro analysis of cold-formed steel members using Abaqus and OpenSees”, *Proceedings of the 13th International Conference on Steel, Space and Composite Structures*, Perth.
- Tsai, K.C., Chen, H.W., Hong, C.P. and Su, Y.F. (1993), “Design of steel triangular plate energy absorbers for seismic-resistant construction”, *Earthq. Spectra*, **9**(3), 505–528. <https://doi.org/10.1193/1.1585727>.
- Whittaker, A.S., Bertero, V.V., Thompson, C.L. and Alonso, L.J. (1991), “Seismic testing of steel plate energy dissipation devices”, *Earthq. Spectra*, **7**(4), 563–604. <https://doi.org/10.1193/1.1585644>.
- Xu, Z.D. (2009), “Horizontal shaking table tests on structures using innovative earthquake mitigation devices”, *J. Sound Vib.*, **325**(1-2), 34–48. <https://doi.org/10.1016/j.jsv.2009.03.019>.
- Xu, Z.D., Ge, T. and Liu, J. (2020), “Experimental and Theoretical Study of High-Energy Dissipation-Viscoelastic Dampers Based on Acrylate-Rubber Matrix”, *J. Eng. Mech.*, **146**(6), 4020057. [https://doi.org/10.1061/\(ASCE\)EM.1943-7889.0001802](https://doi.org/10.1061/(ASCE)EM.1943-7889.0001802).
- Xu, Z.D., Huang, X.H., Xu, F.H. and Yuan, J. (2019), “Parameters optimization of vibration isolation and mitigation system for precision platforms using non-dominated sorting genetic algorithm”, *Mech. Syst. Signal Pr.*, **128**, 191–201. <https://doi.org/10.1016/j.ymsp.2019.03.031>.
- Xu, Z.D., Xu, F.H. and Chen, X. (2016), “Vibration suppression on a platform by using vibration isolation and mitigation devices”, *Nonlinear Dynam.*, **83**(3), 1341–1353. <https://doi.org/10.1007/s11071-015-2407-4>.
- Yousef-beik, S.M.M., Bagheri, H., Veismoradi, S., Zarnani, P., Hashemi, A. and Quenneville, P. (2020a), “Seismic performance improvement of conventional timber brace using re-centring friction connection”, *Structures*, **26**, 958–968. <https://doi.org/10.1016/j.istruc.2020.05.029>.
- Yousef-beik, S.M.M., Veismoradi, S., Zarnani, P. and Quenneville, P. (2020b), “A new self-centering brace with zero secondary stiffness using elastic buckling”, *J. Constr. Steel Res.*, **169**, 106035. <https://doi.org/10.1016/j.jcsr.2020.106035>.

CC